International Journal of Non–Linear Mechanics 159 (2024) 104588

Contents lists available at ScienceDirect

International Journal of Non-Linear Mechanics

journal homepage: www.elsevier.com/locate/nlm

Dynamics of an omnidirectional pendulum energy harvester: A comparative analysis between numerical and experimental results

Philipp Sommermann *, Matthew P. Cartmell

Aerospace Centre of Excellence, Department of Mechanical and Aerospace Engineering , University of Strathclyde, James Weir Building, 75 Montrose Street, Glasgow, G1 1XJ, Scotland, UK

ARTICLE INFO

Keywords:
Spherical pendulum
Nonlinear dynamics
Hardening
Softening
Pendulum energy harvesting
Nonlinear oscillations

ABSTRACT

The spherical pendulum is a mathematically interesting model that has been studied extensively in the past. In the field of energy harvesting however, the pendulum energy harvesters are generally confined to planar motions. This minimisation of the available degrees of freedom potentially limits the areas of application of the energy harvester, and certainly its overall capability. In this work an omnidirectional pendulum energy harvester is proposed in the form of a two degree of freedom system which has the potential to harvest energy from motions along the three axes of translation and from the three corresponding rotations about those axes. The dynamics of such an energy harvester are examined experimentally for different power take-off modes and are subsequently compared to numerical predictions from an analytical model. An optimal operational point is proposed for the harvester and it is shown how an up-sweep and down-sweep of the excitation frequency can significantly broaden the operational range of the energy harvester by up to 130%.

1. Introduction

The work compares some experimental results with the associated numerical predictions for an omnidirectional pendulum energy harvester. The numerical results were based on the solution of a differential equation model which was derived in a previous article that numerically examined the dynamics of the spherical pendulum energy harvester excited in all three orthogonal directions [1]. This numerical analysis was supported by bifurcation diagrams and Poincaré sections and concluded with different graphed results that showed the mean power take-off over the different excitational parameters of the energy harvester. The power take-off term was constructed to model an imposed mechanical load applied to the omnidirectional pendulum energy harvester, operating every half cycle in a manner similar to the approach taken in the work of Watt and Cartmell [2] and McRobb [3]. The previously published article [1] concludes with an optimisation process that was proposed to simplify the selection of optimal excitation parameters for the optimal power output of the pre-prototype. For the numerical examination previously published articles from the literature are found to be of importance. The fundamentals of the dynamics of the spherical pendulum and a simple pendulum with different forcing conditions can be attributed to Miles [4–7] and they were subsequently examined by Olsson [8,9]. Tritton examined the trajectories of the experimentally forced spherical pendulum [10]. Other experimental studies on the spherical pendulum were undertaken by Markeyev [11] and Pospíšil, Fischer and Náprstek [12]. Articles in which observations of chaotic or quasi-periodic dynamics were carried out for the spherical pendulum are attributable to Bryant [13], Kana and Fox [14], Cartwright, Julyan, and Tritton [15], Náprstek and Fischer [16], Litak et al. [17], and Leung and Kuang [18].

The experimental rig that was used for this work applies the principle of electromagnetic energy conversion [19] in the form of two DC motor-generators arranged in such a way that they can be used to convert the angular motions of the pendulum into electrical energy. As the direction of rotation of the DC motor-generators changes periodically a form of rectification is required to get a useful form of electrical energy output. The works of Vullers et al. [20], Shen, Qiu, and Balsi [21], Chen et al. [22], and Elmes et al. [23] discuss the implementation of electrical rectification for vibration-based energy harvesters. Noteworthy previous work in the field of energy harvesting that incorporated an experimental or numerical analyses of a simple pendulum energy harvester was published by Borowiec et al. who examined a pendulum energy harvester excited by random white noise [24]. Cartmell and Lawson showed that unwanted vibration could be absorbed with an absorber element in the form of an inverted pendulum by arranging for autoparametric interaction between two oscillating components [25]. The energy harvesting from a parametrically forced pendulum in a vertical direction was examined by Marszal et al. [26]. An electromagnetic

* Corresponding author.
E-mail addresses: philipp.sommermann@strath.ac.uk (P. Sommermann), matthew.cartmell@strath.ac.uk (M.P. Cartmell).

https://doi.org/10.1016/j.ijnonlinmec.2023.104588
Received 20 August 2023; Received in revised form 28 October 2023; Accepted 14 November 2023
Available online 20 November 2023
0020-7462/© 2023 The Author(s). Published by Elsevier Ltd. This is an open access article under the CC BY-NC-ND license (http://creativecommons.org/licenses/by-nc-nd/4.0/).

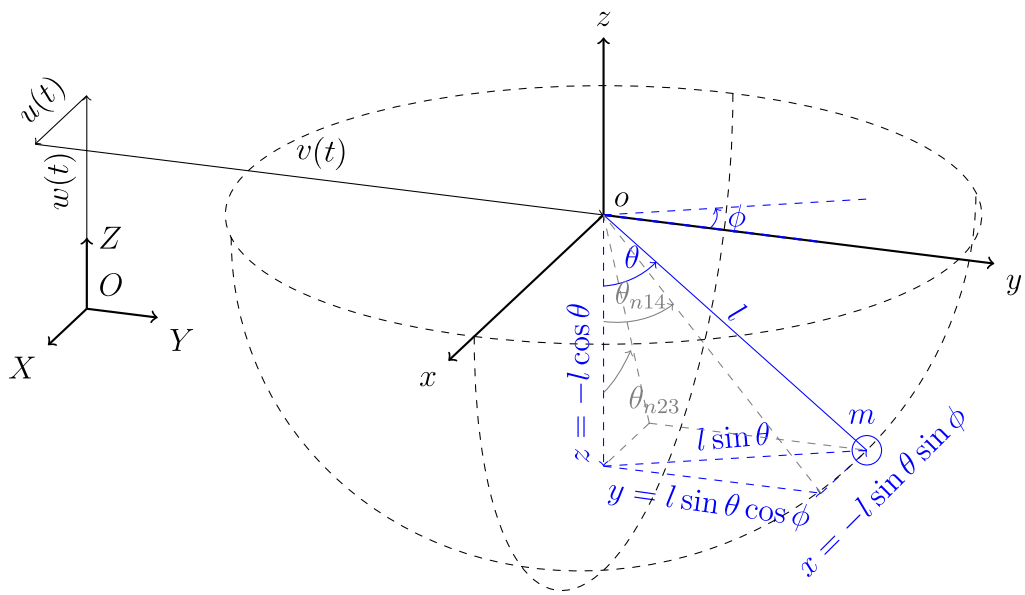

Fig. 1. Diagram of a spherical pendulum with the kinematic relations and the conversion of numerical coordinates θ and ϕ to the numerically calculated and transformed experimental coordinates θ_{n14} and θ_{n23} and showing the limits of the spherical motion reached by the bob (dotted line).

pendulum energy harvester that mechanically rectifies the motion was introduced by Liang et al. [27]. A counterweight pendulum energy harvester excited in a horizontal direction was proposed by Graves et al. [28]. Zhang et al. examined an autoparametric pendulum energy harvester [29].

Spherical pendulum energy harvesters are represented less frequently in the literature compared to simple pendulum energy harvesters. Anurakpandit, Townsend and Wilson [30] observed that as well and noted that a two degree of freedom pendulum energy harvester potentially has the ability to harvest more of the excitational energy. Moreover, efficient energy harvesting is possible regardless of the direction of excitation. Anurakpandit, Townsend and Wilson proposed a gimballed pendulum energy harvester with two degrees of freedom and examined it experimentally and numerically [30]. Another interesting concept for a pendulum energy harvester was the biaxial-pendulum introduced by Wang, Lou, and Zhu [31]. The design of the pendulum energy harvester incorporated two shafts and therefore allowed unrestricted movement of the hemispherically shaped pendulum. The energy was converted to electricity by coils and magnets that were fitted to the hemispherically shaped pendulum. The system was excited by a six degree of freedom platform, and even with an arbitrary excitation direction and excitation frequency the energy harvester showed an energy output.

It is evident that single degree of freedom energy harvesters are disproportionately present in the literature when compared with those exploiting more degrees of freedom. This gap is addressed in the work presented in this article in which an omnidirectional pendulum energy harvester, whose dynamics can be represented by two generalised coordinates, is investigated experimentally. The responses of the experimental system are subsequently compared with theoretical results obtained from numerical integrations of the derived nonlinear ordinary differential equations.

2. Methodology

2.1. Mathematical model

The derivation of the mathematical model for the omnidirectional pendulum energy harvester with an active power take-off term is summarised in an earlier journal article related to this work [1].

In Fig. 1 the schematic model of the spherical pendulum energy harvester is shown. The local coordinate system (o, x, y, z) is attached to the pivot of the pendulum. The excitations $u(t)$, $v(t)$, and $w(t)$ are referred to the global coordinate system (O, X, Y, Z). The excitations are defined with the excitation frequencies by the symbols Ω_u, Ω_v, and Ω_w and the excitation amplitudes with U_0, V_0, and W_0. θ and ϕ are the generalised coordinates chosen for the numerical calculations. They are defined with the necessary kinematic relations shown in Fig. 1. In the figure the length l of the pendulum arm and the mass m of the pendulum bob is shown. Additionally, another pair of coordinates θ_{n14} and θ_{n23} are shown in Fig. 1. Generalised coordinates θ_{n14} and θ_{n23} relate directly to the experimental model, on the basis that this system uses two offset orthogonal shafts to provide the necessary geometrical freedom for spherical motion, within the practical constraints of building a properly functioning system in the laboratory. The subscript n indicates that these coordinates are also used in the numerical analysis, for direct comparison purposes. This subscript is absent on the coordinates associated with the experimental system. The relation between the numerical and experimental coordinates is shown in Eqs. (1) and (2).

$$\theta_{14} = \theta_{n14}. \tag{1}$$

$$\theta_{23} = \theta_{n23}. \tag{2}$$

This notation allows a clear distinction to be made between discussions involving the experimental coordinates and the coordinates that are attributed to the numerical calculation. By observing the kinematic relations in Fig. 1 the generalised coordinates θ and ϕ can be transformed in the coordinates θ_{n14} and θ_{n23}, see Eqs. (3) and (4).

$$\theta_{n14} = \theta \sin(\phi). \tag{3}$$

$$\theta_{n23} = \theta \cos(\phi). \tag{4}$$

The dimensionless ordinary differential equations for the omnidirectional pendulum energy harvester were derived by assembling the potential and kinetic energy expressions based on the kinematic relations shown in Fig. 1 and subsequently by substituting them appropriately into Lagrange's equation of the second kind. This gives the differential Eqs. (5) and (6). Where the parameters ξ_θ and ξ_ϕ define the damping ratios, the parameter ω_n defines the linear undamped natural frequency, and the parameter T_θ defines the power take-off torque.

For a detailed summary of the derivation of the ordinary nonlinear differential equations of motion for the system the preceding article [1] and PhD Thesis (Chapter 4) [32] is recommended.

$$\begin{aligned}
&\ddot{\theta}(t) + 2\xi_\theta \omega_n \dot{\theta}(t) + \frac{g}{l}\sin(\theta(t)) \\
&- \sin(\theta(t))\cos(\theta(t))\dot{\phi}(t)^2 = \\
&- \frac{U_0\Omega_u^2}{l}\cos(\theta(t))\sin(\phi(t))\cos(\Omega_u t) \\
&+ \frac{V_0\Omega_v^2}{l}\cos(\theta(t))\cos(\phi(t))\cos(\Omega_v t) \\
&+ \frac{W_0\Omega_w^2}{l}\sin(\theta(t))\cos(\Omega_w t) \\
&- \frac{2T_\theta}{\pi m l^2}\tan^{-1}\left(\frac{\dot{\theta}(t)}{0.01}\right).
\end{aligned} \tag{5}$$

$$\begin{aligned}
&\ddot{\phi}(t) + \frac{2\xi_\phi\omega_n}{\sin^2(\theta(t))}\dot{\phi}(t) + \frac{2\dot{\theta}(t)\cos(\theta(t))\dot{\phi}(t)}{\sin(\theta(t))} = \\
&- \frac{U_0\Omega_u^2\cos(\phi(t))\cos(\Omega_u t)}{l\sin(\theta(t))} \\
&- \frac{V_0\Omega_v^2\sin(\phi(t))\cos(\Omega_v t)}{l\sin(\theta(t))}.
\end{aligned} \tag{6}$$

To avoid scaling effects dimensionless parameters are introduced, see Eq. (7).

$$\begin{aligned}
&\tau = \omega_0 t, && \omega_0^2 = \tfrac{g}{l}, && P_\theta = \tfrac{T_\theta}{m l^2 \omega_0^2}, \\
&a_u = \tfrac{U_0}{l}, && a_v = \tfrac{V_0}{l}, && a_w = \tfrac{W_0}{l}, \\
&\beta_v = \tfrac{\Omega_v}{\omega_0}, && \beta_w = \tfrac{\Omega_w}{\omega_0}, && \beta_u = \tfrac{\Omega_u}{\omega_0}, \\
&\alpha_\theta = 2\xi_\theta\tfrac{\omega_n}{\omega_0}, && \alpha_\phi = 2\xi_\phi\tfrac{\omega_n}{\omega_0}.
\end{aligned} \tag{7}$$

These as-derived equations are then nondimensionalised to give the dimensionless ordinary differential equations in terms of the coordinates θ in Eq. (8) and ϕ in Eq. (9).

$$\begin{aligned}
&\ddot{\theta}(\tau) + \alpha_\theta\dot{\theta}(\tau) + \sin(\theta(\tau)) \\
&- \sin(\theta(\tau))\cos(\theta(\tau))\dot{\phi}(\tau)^2 = \\
&- a_u\beta_u^2\cos(\theta(\tau))\sin(\phi(\tau))\cos(\beta_u\tau) \\
&+ a_v\beta_v^2\cos(\theta(\tau))\cos(\phi(\tau))\cos(\beta_v\tau) \\
&+ a_w\beta_w^2\sin(\theta(\tau))\cos(\beta_w\tau) - \frac{2P_\theta}{\pi}\tan^{-1}\left(\frac{\dot{\theta}(\tau)}{\epsilon_r}\right).
\end{aligned} \tag{8}$$

$$\begin{aligned}
&\ddot{\phi}(\tau) + \frac{\alpha_\phi}{\sin^2(\theta(\tau))}\dot{\phi}(\tau) + \frac{2\dot{\theta}(\tau)\cos(\theta(\tau))\dot{\phi}(\tau)}{\sin(\theta(\tau))} = \\
&- a_u\beta_u^2\frac{\cos(\phi(\tau))}{\sin(\theta(\tau))}\cos(\beta_u\tau) \\
&- a_v\beta_v^2\frac{\sin(\phi(\tau))}{\sin(\theta(\tau))}\cos(\beta_v\tau).
\end{aligned} \tag{9}$$

2.2. Experimental rig

The experimental rig with the omnidirectional pendulum energy harvester is shown in Fig. 2. In Fig. 2(b) the pivoting suspension and power-take-off sub-systems are shown, these being the most critically important components of the harvester. The power-take-off consists of four small electric generators with coaxial gearboxes and integrated shaft encoders. There is one symmetrically configured pair of generators per axis, and the electrical loads presented by the generators act back on the harvester as mechanical loads on each shaft. The two shafts are designated by subscripts 14 and 23 and their axes are orthogonal. The experimental rig was built with a limited budget and therefore the motivation for this experiment was mechanical simplicity and economy. To that end a sensible design was selected that uses the two shafts already described and is therefore represented by the two coordinates θ_{14} and θ_{23}. The pendulum pivot and power take-off system is mounted within a protective steel cage to provide a highly rigid support. The energy harvester is attached to a shaker table supplied by *Centrotecnica* SRL and this is shown in Fig. 2(a). The shaker table can excite test objects through excitation frequencies from static up to 100 Hz. The maximum excitation amplitude of 14.3 cm is given by the physical restrictions of the linear motors in the shaker table. Noting that the maximum excitation amplitude can only safely be reached for test objects that are small in mass and size and for low excitation frequencies. Because of the large mass and the geometrical size of the energy harvester rig, noting its overall dimensions of 0.75 m × 0.75 m × 1.12 m, the maximum excitation parameters cannot be achieved and the maximum excitation amplitude is therefore restricted to a value of 5.0 cm. This is still sufficient to run the harvester properly and to generate results of considerable interest. The energy harvester's pendulum arm has a length of 0.35 m. The pendulum length is a pragmatic choice made in line with the adopted overall scaling of the experimental rig. The bob mass slightly exceeds 1 kg, at a nominal 1.32 kg, and this ensures that sufficient restoring torque is available, even at the lowest velocities. The pendulum rod can be easily replaced to adapt the energy harvester to other excitation frequencies, and pendulum lengths from 0.1 m to 0.75 m can be accommodated within the framework of the system. The damping ratio is solely attributed to the friction within the energy harvester and a tiny amount of aerodynamic dissipation. The calculation of the damping ratio is achieved by observing the oscillation decay process for each shaft and then obtaining the damping ratios from the calculated logarithmic decrement. The measured damping ratios are $\xi_{14} = 0.0373$ and $\xi_{23} = 0.0339$, respectively. The power take-off in the high power take-off mode is entirely represented by the last term in Eq. (8).

In this work, both low and high power take-off modes are examined. The defining difference between these two modes is based on the amount of energy that is converted within the energy harvester. A load-resistor is connected to each generator for this purpose, see Fig. 3. Values of 10 kΩ for the low power take-off mode and 10 Ω for the high power take-off mode are selected. The terms high and low power take-off are therefore just extremes of a continuum. We note that the term 'mode' as used here does not imply a flexural mode of vibration and instead refers to a basis of operation. The circuit in Fig. 3 shows a voltage divider, see the blue double dotted dashed frame, that is used to measure the voltage output. With both switches (S1 and S1) being opened, as shown in Fig. 3, the parallel series resistor is disconnected and therefore the energy harvester operates in the low power take-off mode, see the green dotted dashed frame. The load resistor (R_S) and the resistors for the voltage bridge divider are in line in this setup. Therefore, the total resistance in the low power take-off mode is $R_{\text{low}} = 47.5$ kΩ. With this high total resistance the overall current output is very small. For the high power take-off mode both switches (S1 and S2) are closed, see the purple dotted frame. This results in a shortening of the resistor R_S and additionally, the current is divided between both branches in the circuit. With the resistors in the different branches being parallel the overall resistance of the circuit has a value of $R_{\text{high}} = 9.997$ Ω in the high power take-off mode. This results in a high current output and therefore a high power output of the energy harvester. The circuit shown in Fig. 3 is used for each individual generator. Note that because of the different resistor values the voltage output V_{out} needs to be multiplied in the microcontroller by a factor of 5 in the high power take-off mode and by 6.33 in the low power take-off mode. Additionally, the current is measured once for each shaft right after the output of the generators 3 and 4 and in front of the shown circuit. After the post-processing of the voltage output as described in Fig. 9 the power output of the energy harvester for each shaft is calculated with Eq. (10).

$$P_{14} = 2\,V_{14}\,I_4, \quad P_{23} = 2\,V_{23}\,I_3. \tag{10}$$

Fig. 4 shows the top view of the omnidirectional pendulum energy harvester mounted on the shaker table. The cage of the omnidirectional pendulum energy harvester has been removed to increase clarity. The

(a) Omnidirectional pendulum energy harvester mounted on a shaker table

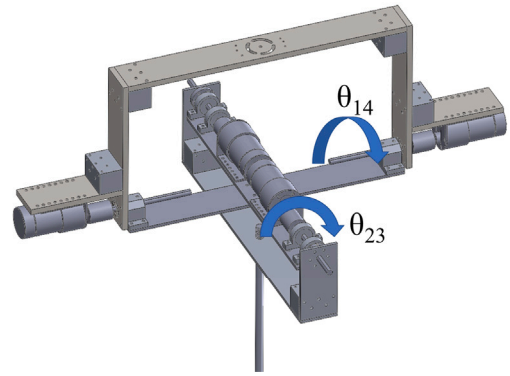

(b) CAD drawing of the pendulum pivot and power take-off system with the coordinates θ_{14} and θ_{23}

Fig. 2. Experimental rig.

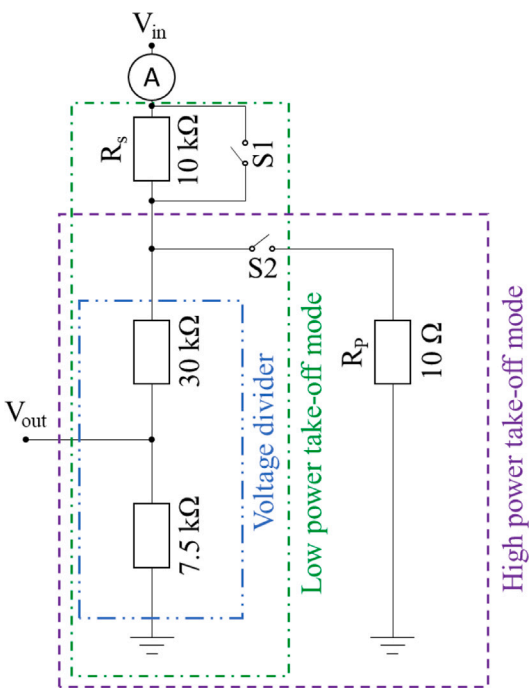

Fig. 3. Circuit defining the low and high power take-off modes and the measurement positions for voltage and current.

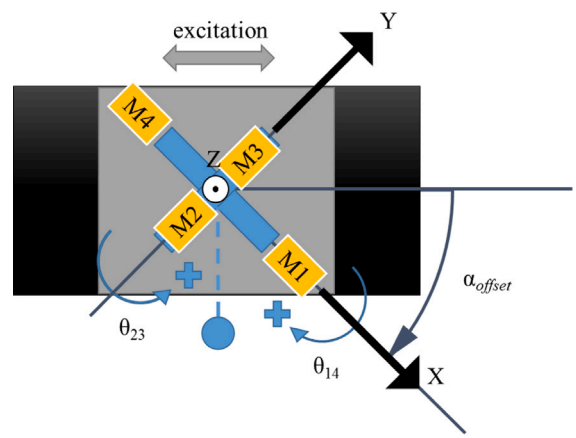

Fig. 4. Top view of the experimental rig mounted on the shaker table with the pendulum deflected to the bottom.

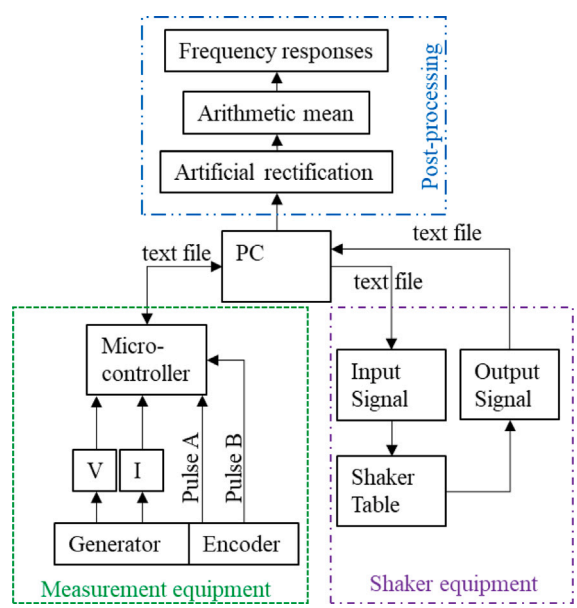

Fig. 5. Block diagram of the microcontroller, shaker table, and post-processing process.

shaker table excites the system horizontally, as shown in Fig. 4 . The two shafts (shaft 14 and shaft 23) and their corresponding coordinates θ_{14} and θ_{23} are shown in Fig. 4 . The motor-generators M1 to M4 are connected to the shafts. The generators M1 and M2 are used as points of reference to define the direction of rotation for the coordinates. This means that when the pendulum bob is deflected, as shown in Fig. 4, in a positive x-direction and a negative y-direction both coordinates show a positive deflection value. Another adjustment parameter is the offset angle α_{offset} which defines the static angular position by which the omnidirectional pendulum energy harvester is mounted on the shaker table. An offset angle of 0° is equivalent to a simple pendulum energy harvester where the only oscillating shaft is shaft 23, and with an offset angle of 90° a simple pendulum energy harvester is observed where only shaft 14 is oscillating. Therefore, for the work reported in this article the offset angle is set to a value of 45°, as shown in Fig. 4 to ensure participation of both shafts.

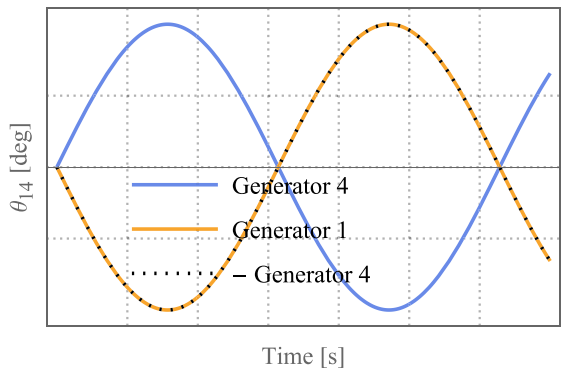

Fig. 6. Qualitative deflection values of the generators 1 and 4.

Fig. 5 shows a block diagram for the experimental equipment and the post processing. The figure shows one of the four generators and encoders as an example connected to the microcontroller. The personal computer connects the shaker table with a CAN to a USB cable, see the purple dotted dashed frame. This transfers the input signal as a text file to the shaker table. After the excitation process is performed the shaker table sends back an output signal giving the real position of the shaker table at any point during the experiment. Additionally, the computer is connected to a suitable microcontroller, which is connected to the voltage bridges, see Fig. 3, and the encoders, see dotted green frame. The microcontroller processes the input signals and gives a text file as output with different columns for time, encoder position, voltage, and current output for different generators. These files are then used in the post-processing, see the blue double dotted dashed frame, to create frequency responses as described in greater detail in the following.

2.3. Post-processing of the experimental data

The generators are connected to a suitable microcontroller that measures the output voltage of each of the generators. Additionally, the generators are equipped with inbuilt encoders that measure the angular deflections of each of the generator shafts. The microcontroller stores the pulse trains from the encoder and gives an output of the summed-up encoder values every 12 ms. This rate of repetition is a result of the limiting factor of the microcontroller the baud rate.

Since the two generators on each shaft are facing each other the output of each of the encoders and measured voltage are oppositely signed. This results in a phase shift between the two generator values that needs to be addressed, this work uses an artificial post-processing process. Fig. 6 is used to describe this process. It shows the deflection values of generator 4, generator 1, and the additive inversed deflection of generator 4. Note that in this work it is defined that the output values of the generators 3 and generators 4 are always those additive inversed. With this inversion the deflection over time outputs of the generators on the shaft does not have a phase shift anymore. They are subsequently arithmetically averaged to get the overall deflection value of shaft 14 the coordinate θ_{14}. The same procedure is used with the deflection values connected to shaft 23. For the voltage output values the same artificial procedure is applied, this is discussed later see Fig. 9.

The experimental data is processed and the frequency responses are shown in the results section, see Figs. 11 and 12 which is discussed later. Some clarifications need to be made here about the process behind the generation of the figures. The frequency responses contain three different parts the linear part of the frequency response, the lower nonlinear jump region and the upper nonlinear jump region, see Fig. 11. The are determined with three different measurement methods and are shown with different symbols and colours in the frequency responses. The post-processing process to obtain these regions is described in greater detail in the following. The linear part of the frequency response (blue circles) is measured with an excitation input signal that applies a constant excitation frequency (Ω) for 200 s, see Fig. 7(b). Afterwards, the maximum and additive inversed minimum deflection values of the coordinates θ_{14} and θ_{23} are arithmetically averaged over the last 20 s to remove unwanted transient features of the response and emphasise the more persistent steady-state features instead, see Fig. 7(a). It is clear that the transient response characteristics are no longer present. In Fig. 7(b) the excitation frequency is shown over time. It is visible that the excitation frequency is held at a constant level for the whole experiment. These measurements are repeated at least once. These arithmetically mean maximum deflection values from each individual measurement are stored into a data file for the frequency response, and then the response for the next excitation frequency is measured. This process is repeated until the pre-defined frequency range has been captured. This averaging over twenty seconds ensures that the measurement points all represent steady-state response values. Henceforth these frequency responses are referred to as the linear part of the frequency responses or linear frequency response. The other two types of points shown in the figures are frequency down-sweeps (orange triangles) and frequency up-sweeps (red diamonds) where the excitation frequency is reduced or increased, at a constant linear rate, see Fig. 8. These results then form the lower and upper nonlinear jump regions in the frequency responses, see Fig. 11. Note that the defining parameter is the time period of the sweep, in this case 200 s. This results in a changing sweep rate depending on the starting and end frequency of the sweep. Mathematically for a determination of jump down points the sweep rate needs to be infinitesimal low. Unfortunately, practically this is not possible therefore the following sweep rates are selected as a compromise. The sweep rate for the low power take-off mode is −0.012 Hz/min for the down-sweep and 0.039 Hz/min for the up-sweep. In the high power take-off mode the sweep rate for the down-sweep is −0.024 Hz/min and 0.042 Hz/min for the up-sweep. Subsequently, the up- and down-sweeps are divided into twenty elements. Fig. 8(a) shows the division of an up-sweep in twenty elements as an example for the coordinate θ_{23}. In Fig. 8(b) the linear increase of excitation frequency over time is shown. The excitation time signal is divided into twenty elements and the elements are then subsequently mirrored with the linear increase of the excitation frequency and therefore transform into frequency bandwidth elements. This shows that an element in the time domain can directly be transformed to the bandwidth element in the frequency domain for a linear increase in the excitation frequency during the sweep. To consider an example, in Fig. 8(a) the energy harvester is excited with a frequency up-sweep with a starting frequency of 0.82 Hz and an end frequency of 0.96 Hz. The difference between the two excitation frequencies is therefore $\Delta\Omega = 0.14$ Hz. Because of the previously mentioned linear increase rate of the excitation frequency over the 200 s of excitation period $\Delta\Omega$ can be divided by 20, which is the quantity of the bandwidth elements. Therefore, a bandwidth element has a value of 0.007 Hz. Subsequently, the maximum and additive inversed minimum deflections of the experimental coordinates are stored and then arithmetically averaged for each bandwidth element. The result of this calculation is the maximum deflection at the position in the middle between the two borders of the bandwidth element. At the start of the frequency sweeps the dynamics of the energy harvester undergo a transient response and therefore in some cases the deflection output is lower or higher than in the linear frequency response, see Fig. 8(a) as an example. These points that clearly can be attributed to the transient dynamics are shown in the experimental result figures for the sake of completeness but are not discussed in greater detail since they do not directly affect the operational range of the energy harvester. The starting points of the sweeps are marked with black circles, see Figs. 11 and 12. The linear operational range is defined as the frequency range between the two local maxima of the frequency response for the coordinate θ_{14}, see Fig. 11(a) where this is discussed in greater detail. The linear operational range is branded by the presence

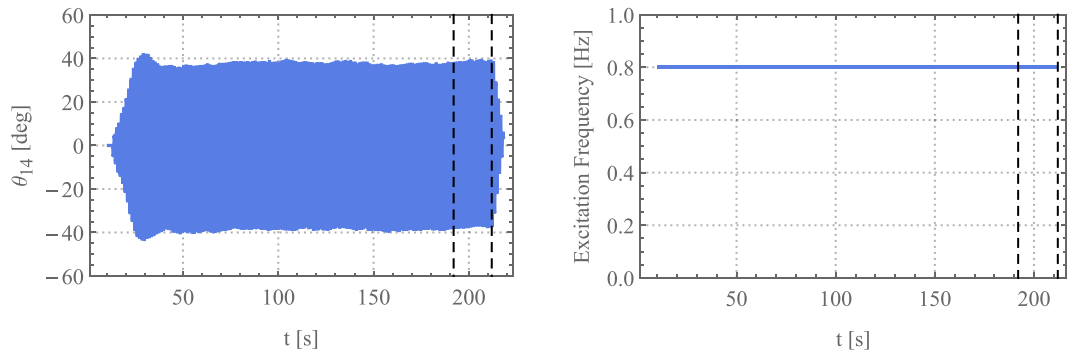

(a) Deflection of θ_{14} over time (b) Excitaiton frequency over time

Fig. 7. Definition of the time period to calculate the linear part of the frequency response.

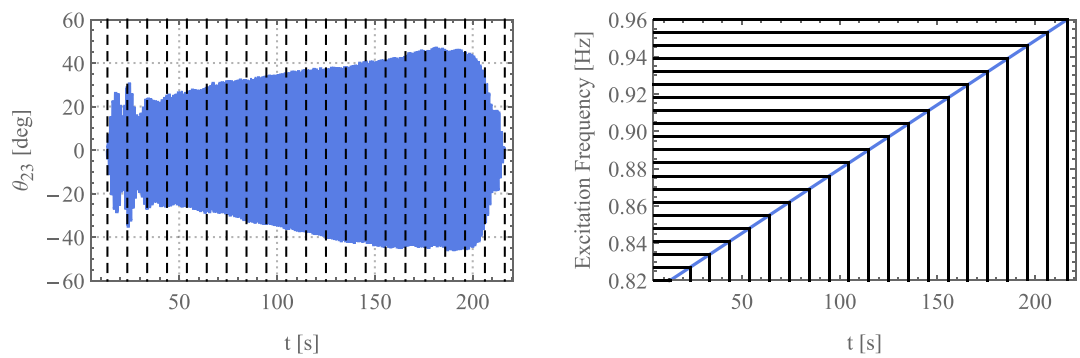

(a) Deflection of θ_{23} over time (b) Excitaiton frequency over time

Fig. 8. Definition of the bandwidth element for the up- and down-sweeps, shown here up-sweep 0.82 Hz to 0.96 Hz.

of the lower and upper nonlinear jump region, which occur because of frequency sweeps. Since the absolute values of these jump regions and linear operational range are low in value a dimensionless quantity is introduced in Fig. 11 to see the broadening more user-friendly in per cent. In accordance with the previously mentioned definition the linear operational range in the low power take-off is 0.08 Hz wide and in the high power take-off mode it is 0.11 Hz wide. These values are used as the basis for the calculation of the broadening of the up- and down-sweeps in percentage terms, see Eqs. (11) and (12).

$$\text{Broadening}_{\text{down-sweep}} = \frac{\text{Lower jump region}}{\text{Linear operational range}}\ 100. \tag{11}$$

$$\text{Broadening}_{\text{up-sweep}} = \frac{\text{Upper jump region}}{\text{Linear operational range}}\ 100. \tag{12}$$

The post-processing for the voltage output is similar to the one of the deflection values. There are subtle differences however which are discussed in the following. The measuring position of the voltage output for each of the generators is shown in Fig. 3. The microcontroller however can only measure positive voltage output. To get an oscillating signal for V_{14} the opposing orientation of the two generators of the shaft is used. When the voltage output of generator 1 shows a voltage output the voltage output of generator 4 shows in theory the additive inversed value. Since negative values unfortunately cannot be measured with this setup, the output that the microcontroller shows for generator 4 is equal to zero and vice versa. This can be exploited in order to artificially construct a voltage output value for the shaft. This is done by subtracting the voltage output of generator 4 from the voltage output of generator 1 $V_{14} = V_1 - V_4$. This gives an oscillating voltage output signal for the shaft with the direction of oscillation being equivalent to the defined direction of rotation. The same procedure is done with the generators 2 and 3 where the voltage output of generator 3 is subtracted from the voltage output of generator 2. In Fig. 9 the post processing of the voltage output V_{14} as an example. The voltage output V_{14} is artificially rectified in a first step. This artificial process mimics a diode rectification as shown in Fig. 9(b). Afterwards the arithmetic mean is calculated from the rectified voltage output. This is done over the in Figs. 7 and 8 defined bandwidth elements and steady-state elements. In a further step the frequency responses for the voltage outputs with the inclusion of the up- and down-sweeps are created as described previously. The arithmetic mean rectified value is indicated in the frequency responses with the notation 'avg.'. The authors selected an arithmetic mean rectified voltage over a RMS voltage to show that the AC-voltage output of the energy harvester is artificially undergoing a rectification progress to a DC-voltage, see Fig. 9(b). With the factor form the RMS values can be calculated, for a sine function this is calculated with $RMS(V_{14}) = avg.V_{14} \times 1.11$ [33].

It is important to note that the voltage output of a DC generator is dependent on the rate of revolution and therefore on the velocity [34, 35]. Therefore, it is possible that the global maximum deflection value is not at the same position as the global maximum voltage output. This is shown in greater detail in the results section in Fig. 12. The linear relation between the arithmetic mean rectified velocity of the coordinate θ_{14} over the arithmetic mean rectified voltage output V_{14} is shown in Fig. 10. The data used for this plot is taken from Figs. 12(c) and 12(e). To only observe the relation between the avg. $\dot{\theta}_{14}$ and avg. V_{14} in the operational area it is defined that voltage outputs with a value lower than 1.4 V are not observed. The trend line and function of the relationship between avg. $\dot{\theta}_{14}$ and avg. V_{14} is calculated with a linear fit model and shown in Fig. 10.

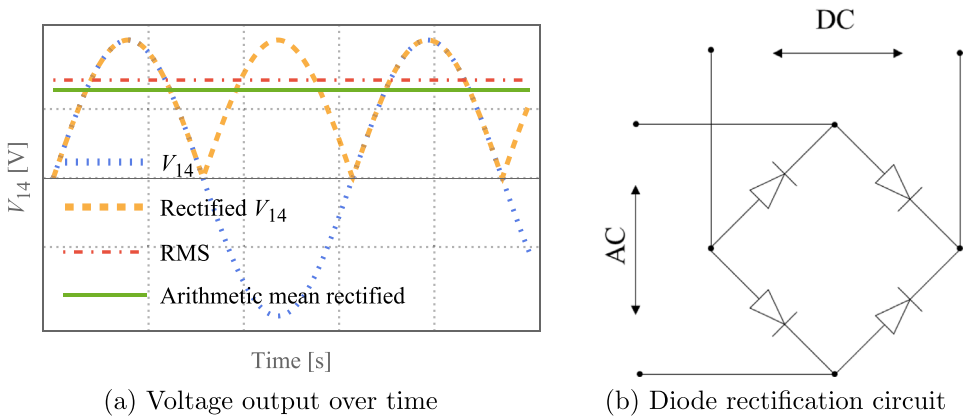

(a) Voltage output over time (b) Diode rectification circuit

Fig. 9. Definition of the voltage output of the energy harvester.

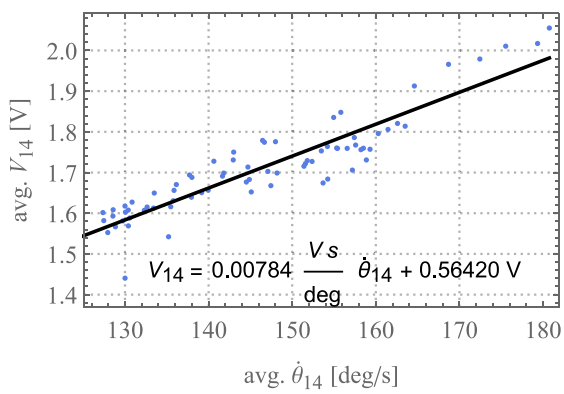

Fig. 10. Arithmetic mean rectified voltage over arithmetic mean rectified velocity of shaft 14 in the high power take-off mode.

3. Results

3.1. Experimental results

In Fig. 11 frequency responses of the coordinates θ_{14} and θ_{23} and the associated arithmetic mean rectified voltage outputs for the energy harvester are shown. The two parameters were selected for practical reasons. From a design point of view it is crucial to know the maximum deflections of the shafts to build the protective cage with enough clearance for the pendulum bob to prevent a collision. Additionally, the voltage output is needed for the calculation of the power output of the energy harvester. Note that the velocity of the coordinates θ_{14} and θ_{23} is proportional to the voltage output V_{14} and V_{23}, see Fig. 10. The crucial point here to note that it is observed that in the linear operational range and the lower and upper nonlinear jump region an increase in the excitation frequency dose increase the oscillation frequency of the pendulum. The resistor value was selected so that the energy harvester is operating initially in the low power take-off mode. The omnidirectional pendulum energy harvester is excited with an excitation amplitude of $A = 32$ mm, this is the maximum excitation amplitude that can safely be used with the harvester rig, as set up, before internal collisions occur.

In Fig. 11(a) the frequency response for the coordinate θ_{14} is shown. The linear operational region (blue arrow) is defined as the area between the two maxima of the linear part of the frequency response of the coordinate θ_{14}. In this region the coordinate θ_{14} of the energy harvester shows high deflections and therefore the efficiency of the energy harvester is high. As mentioned before the linear operational range is the area to which the upper and lower nonlinear jump regions are referred to in order to calculate the broadening, see Eqs. (12) and (11). The bandwidth and position of the linear operational range of the coordinate θ_{14} is directly applied to the coordinate θ_{23} for reasons of simplicity.

The frequency response for the coordinate θ_{14} is shown in Fig. 11(a). The linear part of the frequency response (blue circles) shows a steep rise in deflection for an excitation frequency from 0.75 Hz to 0.78 Hz. The maximum deflection for the coordinate θ_{14} of 43.20° is reached at an excitation frequency of 0.78 Hz. With a further increase in the excitation frequency the deflection of the coordinate θ_{14} decreases and shows a local minimum of 32.29° at a value for the excitation frequency of 0.84 Hz. After the local minimum is passed the deflection continues to increase and reaches a local maximum deflection of 34.85° for an excitation frequency value of 0.86 Hz. With a further increase in the excitation frequency the deflection of the coordinate θ_{14} jumps down to a value of 17.76° and continues to decrease as the excitation frequency increases. The down-sweep (orange triangles) starts at an excitation frequency of 0.789 Hz where the coordinate θ_{14} shows a deflection value that is lower than the linear frequency response. The following deflection values of the down-sweep are slightly higher than the linear frequency response. Additionally, the higher deflection is visible for a broader range of the excitation frequencies. The maximum deflection of the down-sweep of 51.58° is reached at a value of the excitation frequency of 0.763 Hz and is, therefore, 0.017 Hz lower than at the lower limit of the linear operational range. This is equivalent to a broadening of the operational range of 21.25%, as defined in Eq. (11). These softening characteristics are typical of the dynamics of a pendulum based system. The starting point of the up-sweep (red diamonds) is at an excitation frequency of 0.84325 Hz. With an increase in the excitation frequency the deflection of the coordinate θ_{14} increases and reaches its maximum deflection of 47.97° at a value of the excitation frequency of 0.94725 Hz. Therefore, the up-sweep broadens the operational range by 0.08725 Hz which is equivalent to 109.06% broadening, see Eq. (12) where the linear operational range is used as base value. After the maximum deflection is passed the deflection slightly decreases until jumping down to a value of 13.84° at a value of the excitation frequency of 0.96025 Hz. With the hardening and softening characteristics of the up- and down-sweep the operational range of the coordinate θ_{14} is overall drastically increased by more than double the base value by 130.31% (0.10425 Hz).

In Fig. 11(b) the frequency response for the coordinate θ_{23} is shown. The linear frequency response (blue circles) sees a rising deflection for the first three measurement points and then the response drops to a value close to zero until the excitation frequency of 0.8 Hz is exceeded. With a further increase in the excitation frequency the deflection of the coordinate θ_{23} rises and reaches its maximum deflection of 36.34° at a value for the excitation frequency of 0.87 Hz. The deflection of the coordinate θ_{23} decreases after the maximum is passed with an

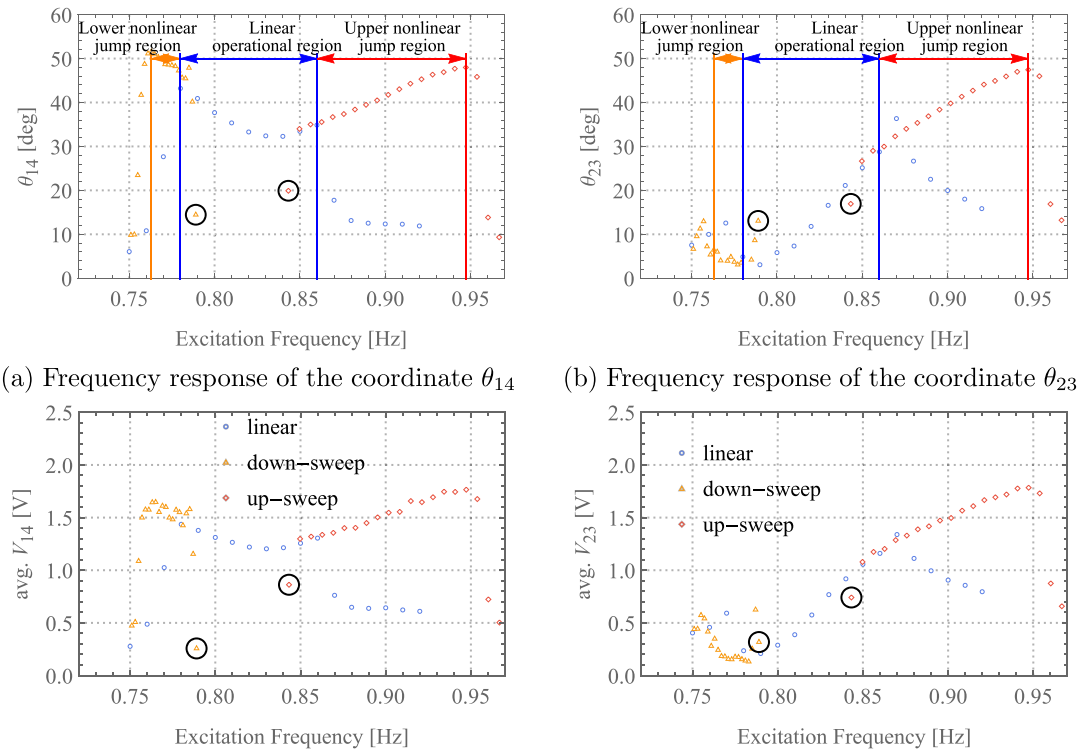

(a) Frequency response of the coordinate θ_{14}

(b) Frequency response of the coordinate θ_{23}

(c) Frequency response of arithmetic mean rectified voltage output of shaft 14

(d) Frequency response of arithmetic mean rectified voltage output of shaft 23

Fig. 11. Frequency responses for the omnidirectional pendulum energy harvester in the low power take-off mode with up- and down-sweeps. The parameters of the omnidirectional pendulum energy harvester are: l = 0.35 m, m = 1.32 kg, α_{offset} = 45°, A = 32 mm, ξ_{14} = 0.0373, and ξ_{23} = 0.0339. (For interpretation of the references to colour in this figure legend, the reader is referred to the web version of this article.)

increase in the excitation frequency. At an excitation frequency of 0.7875 Hz the starting point of the down-sweep is circled in black. With a further decrease of the excitation frequency in the down-sweep the deflection values of the coordinate θ_{23} decrease first and then gradually increase. However, the deflection values of the down-sweep show lower values than the linear frequency response for most of the excitation frequency range during the down-sweep. There is no broadening of the operational area of the coordinate θ_{23} observed during the down-sweep. The up-sweep starts at an excitation frequency of 0.84325 Hz where the deflection of the coordinate θ_{23} shows a lower value than the linear frequency response. When the excitation frequency is increased further the deflection of the coordinate θ_{23} continues to increase and reaches its maximum value of 47.44° at an excitation frequency of 0.94725 Hz. This is at the same position as the maximum deflection of the coordinate θ_{14}. When the excitation frequency in the up-sweep is increased further and after reaching the maximum deflection the deflection decreases slightly in the next measurement point and then jumps down to 16.89° at an excitation frequency of 0.96025 Hz. The up-sweep shows a value for the upper nonlinear jump region of 0.08725 Hz and overall this results in a higher deflection by 11.10°. This is equivalent to a broadening by 109.06% compared to the linear operating range as defined in Eq. (12).

Fig. 11(c) shows the arithmetic mean rectified voltage output of θ_{14} in the frequency domain. The linear part of the frequency response follows the linear frequency response in Fig. 11(a) of the coordinate θ_{14} well. The voltage output shows its first maximum of 1.44 V at an excitation frequency of 0.78 Hz. With a further increase in the excitation frequency the voltage output decreases and reaches a local minimum of 1.20 V at an excitation frequency of 0.84 Hz. The voltage output increases onwards and shows a local maximum of 1.31 V at an excitation frequency of 0.86 Hz. The mentioned voltage maxima and minimum are observed at the same excitation frequency as those of the coordinate θ_{14}. Similar to the linear frequency response the down-sweep shows good accordance with the coordinate θ_{14} and reaches its maximum of the arithmetic mean rectified voltage output of 1.647 V for a value of the excitation frequency of 0.765 Hz. The up-sweep in the voltage output in the frequency domain shows the same characteristics as the up-sweep of the coordinate θ_{14} with the maximum of the arithmetic mean rectified voltage output of 1.77 V reached at the same position as the coordinate θ_{14} at an excitation frequency of 0.94725 Hz. Since the maximum voltage outputs are observed at the same position as the ones for the coordinate θ_{14} the broadening of the operational range is identical.

In Fig. 11(d) the voltage output in the frequency domain for the coordinate θ_{23} is shown. The linear frequency response of the arithmetic mean rectified voltage output (avg. V_{23}) shows similar results to that of the coordinate θ_{23} in Fig. 11(b). The maximum for the arithmetic mean rectified voltage output of 1.34 V is reached at an excitation frequency of 0.87 Hz. The frequency down-sweep starts at an excitation frequency of 0.7875 Hz and follows the down-sweep of the coordinate θ_{23} well. At an excitation frequency of 0.84325 Hz the up-sweep starts. With an increase in the excitation frequency the arithmetic mean rectified voltage output increases and reaches its maximum of 1.78 V for a value of the excitation frequency of 0.94725 Hz at the same position as the maximum deflection of the coordinate θ_{23} and is therefore identical. With a further increase in the excitation frequency the arithmetic mean rectified voltage output decreases slightly and jumps down to a value of 0.88 V in the next step.

Fig. 12 shows frequency responses and the voltage output in the frequency domain for the omnidirectional pendulum energy harvester in the high power take-off mode. Because of the higher power take-off a higher excitation amplitude is needed to see similar deflection values as in the frequency responses for the low power take-off mode. Therefore, the excitation amplitude is set to A = 48 mm. This is the maximum

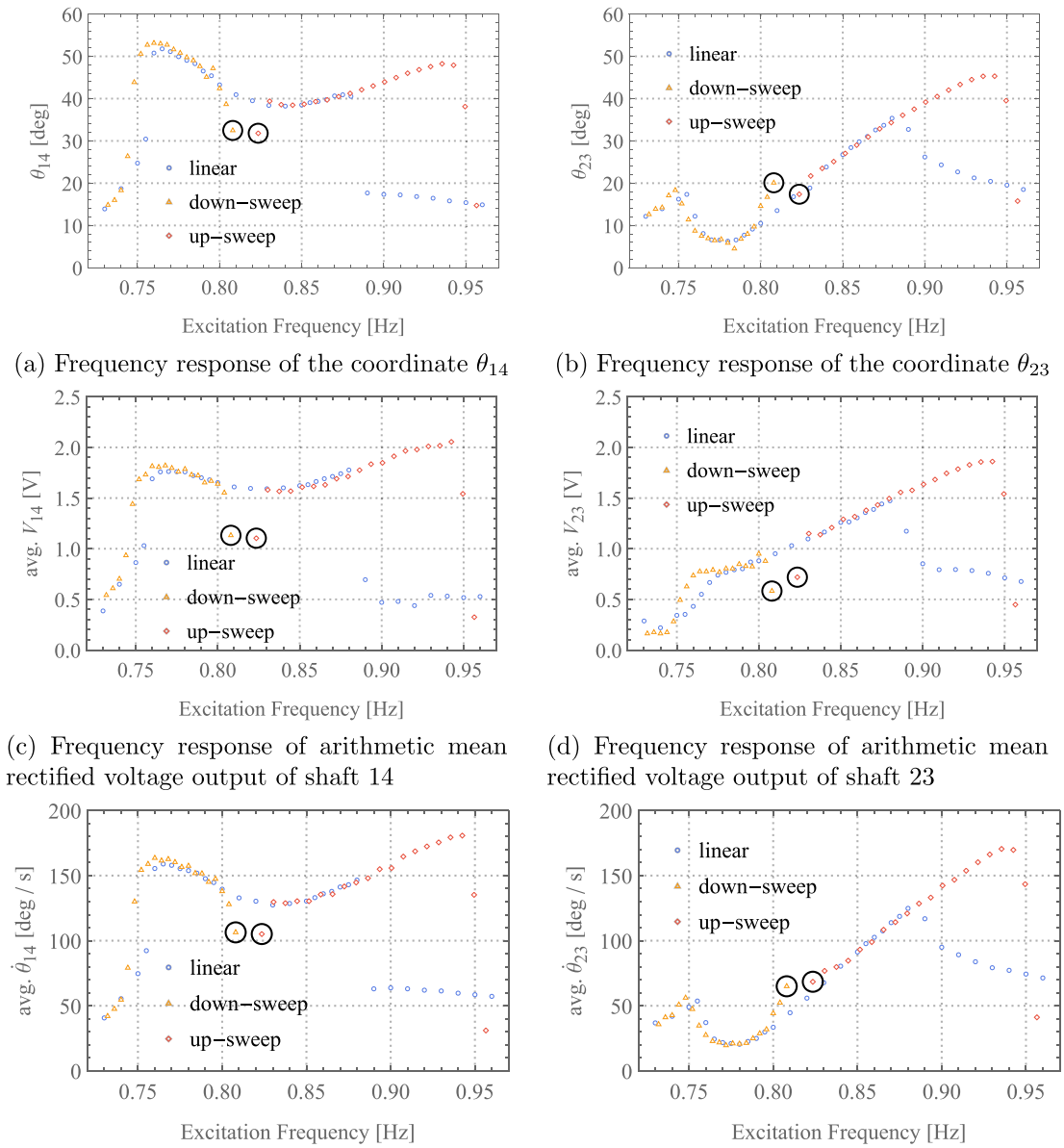

(a) Frequency response of the coordinate θ_{14}

(b) Frequency response of the coordinate θ_{23}

(c) Frequency response of arithmetic mean rectified voltage output of shaft 14

(d) Frequency response of arithmetic mean rectified voltage output of shaft 23

(e) Frequency response of arithmetic mean rectified of $\dot{\theta}_{14}$

(f) Frequency response of arithmetic mean rectified of $\dot{\theta}_{23}$

Fig. 12. Frequency responses for the omnidirectional pendulum energy harvester in the high power take-off mode with up- and down-sweeps. The parameters of the omnidirectional pendulum energy harvester are: $l = 0.35$ m, $m = 1.32$ kg, $\alpha_{offset} = 45°$, $A = 48$ mm, $\xi_{14} = 0.0373$, and $\xi_{23} = 0.0339$.

excitation amplitude that can safely be used with the harvester rig in the high power take-off mode before internal collisions occur. From an energetic point of view the increase in excitation amplitude increases the input energy in the system by a factor of 2.25.

In Fig. 12(a) the frequency response for the coordinate θ_{14} is shown. The linear frequency response sees a steep rise over the first five measurement points and reaches its maximum deflection of 51.77° at an excitation frequency of 0.765 Hz. With a further increase in the excitation frequency the deflection of the coordinate θ_{14} decreases and reaches a local minimum of 38.22° for an excitation frequency of 0.84 Hz. The deflection of the coordinate θ_{14} continues to increase with a further increase in the excitation frequency and reaches a second local maximum of 40.91° at an excitation frequency of 0.875 Hz. The down-sweep of the coordinate θ_{14} starts at an excitation frequency of 0.808 Hz. With a decrease in the excitation frequency the deflection continues to increase and reaches a maximum of 53.14° at an excitation frequency of 0.76 Hz. The down-sweep increases the operational range of the energy harvester slightly by 4.54% (0.005 Hz). The up-sweep starts at an excitation frequency of 0.8235 Hz. With an increase in the excitation frequency the deflection of the coordinate θ_{14} follows the linear frequency response well. When the linear operational range sees a jump down to a smaller deflection value the up-sweep continues to increase in deflection and reaches its maximum deflection of 48.25° at an excitation frequency of 0.9355 Hz. With a further increase in the excitation frequency the deflection decreases slightly and then jumps down to a value of 14.73° in the next step. The upper nonlinear jump region broadened the operational range of the omnidirectional energy harvester by an excitation frequency of 0.0605 Hz and the maximum deflection of the coordinate θ_{14} that is reached is 7.34° higher. This is equivalent to a broadening of the operational range by 55.00%, according to the definition described in Eq. (12). With the lower and upper nonlinear jump regions the operational range of the coordinate θ_{14} shows an overall increase in possible operational range by 59.55%

(0.0655 Hz) compared to the linear operational range used as a base value.

The frequency response of the coordinate θ_{23} is shown in Fig. 12(b). Over the first four measurement points the linear part of the frequency response sees an increase in deflection and reaches a local maximum deflection of 17.36° at an excitation frequency of 0.755 Hz. With a further increase in the excitation frequency the deflection of the coordinate θ_{23} decreases and reaches a minimum deflection of 6.29° at an excitation frequency of 0.78 Hz. The deflection continues to increase with an increase in the excitation frequency and reaches the global maximum deflection of the linear frequency response of 35.63° at an excitation frequency of 0.88 Hz. With a further increase in the excitation frequency the deflection of the coordinate θ_{23} gradually decreases. The starting frequency of the down-sweep is 0.808 Hz. The down-sweep closely follows the linear frequency response. It shows a local maximum of 18.34° at an excitation frequency of 0.748 Hz. The up-sweep starts at an excitation frequency of 0.8235 Hz and follows the linear frequency response of the coordinate θ_{23} well until the maximum of the linear frequency response is exceeded. Onwards from there the up-sweep continues to show an increase in deflection of the coordinate θ_{23} and reaches a maximum deflection of 45.31° at an excitation frequency of 0.9425 Hz. With a further increase of the excitation frequency the deflection of the coordinate θ_{23} decreases first slightly and then jumps down to a value of 15.77°. The upper nonlinear jump region increases the operational range by a value of 0.0625 Hz and the maximum deflection of the coordinate θ_{23} is 9.68° higher than in the linear frequency response. This is equivalent to an increase in the operational range of the coordinate θ_{23} of 61.36% (0.0675 Hz), according to the definition in Eq. (12).

In Fig. 12(c) the arithmetic mean rectified voltage output of the coordinate θ_{14} in the frequency domain is shown. The linear part of the frequency response of the arithmetic mean rectified voltage output V_{14} closely follows the linear frequency response for the coordinate θ_{14} and shows maxima of the arithmetic mean rectified voltage outputs of 1.76 V and 1.77 V at excitation frequencies of 0.77 Hz and 0.88 Hz. The second local maximum of the arithmetic mean rectified voltage output has a higher value. This is as already mentioned in the methodology section and is attributed to the fact that the voltage output depends on the velocity of the coordinate θ_{14}, see Fig. 10. When measuring the oscillation frequency of the coordinate θ_{14} close to the first (left) maximum and comparing it to the second (right) maximum it is evident that at the right maximum the oscillation frequency is higher. With a higher oscillation frequency the velocity of shaft 14 is higher as well. And with a higher velocity a higher voltage output is observed. In between the two maxima a local minimum of 1.59 V at an excitation frequency of 0.83 Hz is observed. The down-sweep of the arithmetic mean rectified voltage output V_{14} follows the deflection of the coordinate θ_{14} well and reaches its maximum arithmetic mean rectified voltage output of 1.81 V for a value of the excitation frequency of 0.76 Hz. Therefore, the broadening of the operational range with the down-sweep shows identical values. The up-sweep of the arithmetic mean rectified voltage output of shaft 14 shows the same characteristics as the up-sweep of the coordinate θ_{14}. It reaches the maximum arithmetic mean rectified voltage output of 2.06 V for a value of the excitation frequency of 0.9425 Hz and is therefore broadened identically to the coordinate θ_{14}.

The arithmetic mean rectified voltage output V_{23} in the frequency domain is shown in Fig. 12(d). The linear part of the frequency response of the arithmetic mean rectified voltage output shows high accordance with the frequency response of the coordinate θ_{23} for the most part. The down-sweep shows similar arithmetic mean rectified voltage outputs as the steady-state response. The up-sweep in the voltage output in the frequency domain shows the same characteristics as the frequency response of the coordinate θ_{23}. The maximum arithmetic mean rectified voltage output of 1.86 V is reached at an excitation frequency of 0.9425 Hz and the broadening of the operational range is therefore identical in position to that of the coordinate θ_{23}.

Additionally, the frequency responses of the arithmetic mean velocity of the two coordinates θ_{14} and θ_{23} of the energy harvester are introduced in Figs. 12(e) and 12(f) to show the relationship between voltage output and velocity of the shafts. Fig. 12(e) shows the velocity of θ_{14} over the excitation frequency. It is evident that the arithmetic mean voltage output V_{14}, in Fig. 12(c) shows the same characteristics as the arithmetic mean of $\dot{\theta}_{14}$. The maximum velocity of the down-sweep has a value of $\dot{\theta}_{14} = 163.507\ \frac{\text{deg}}{\text{s}}$ and the maximum velocity of the up-sweep has a value of $\dot{\theta}_{14} = 180.753\ \frac{\text{deg}}{\text{s}}$. The unit deg/s is used over the SI-unit for the convenience of the reader. The higher maximum value of the up-sweep compared to the down-sweep is observed in the frequency response for the velocity as well, which is similar to the behaviour observed in the frequency response for the voltage output.

In Fig. 12(f) the velocity of the coordinate θ_{23} over the excitation frequency is shown. The frequency response shows the same characteristics as the frequency response of the arithmetic mean voltage output of shaft 23 in Fig. 12(d). The maximum velocity output is observed at the up-sweep and has a value of $\dot{\theta}_{23} = 170.498\ \frac{\text{deg}}{\text{s}}$.

The power output of each shaft can be generated by multiplying the voltage output with the current output. For this calculation it is assumed that the generators are connected in series. The power output is calculated with Eq. (10). Therefore, the arithmetic mean rectified power output at the optimal operational point of 0.9355 Hz has values of $P_{14} = 2.863$ W and $P_{23} = 2.525$ W.

It is important to mention that both power take-off modes of the omnidirectional pendulum energy harvester show operating frequency ranges where the dynamics are similar to those of a simple pendulum. In these areas only shaft 14 is moving and shaft 23 hardly shows any deflection. These dynamics are observed in the vicinity of the first maximum deflection of the coordinate θ_{14} and are therefore for the down-sweep as well. At the second local maximum of the coordinate θ_{14} both shafts show high deflections. When looking at the energy harvester from the top it can be observed the trajectory of the pendulum bob follows an almost circular pattern. Therefore, the dynamics of the omnidirectional pendulum energy harvester appear to be the same as those of a conical pendulum, in the area of the second local maximum of the coordinate θ_{14}. This applies to the complete upper nonlinear jumping region as well.

With the inclusion of the lower and upper nonlinear jump regions the operational range of the energy harvester can be broadened drastically. An optimal operational point of the omnidirectional energy harvester is on, or close to, the maximum deflection of the upper jumping region before the jump down to the small deflection values occurs. In this operational region both shafts show high deflection values, and this results in a high overall power output of the omnidirectional pendulum energy harvester.

3.2. Numerical reconstruction of experimental results

The dimensionless ordinary differential Eqs. (8) and (9) in terms of the generalised coordinate θ and ϕ are solved using a suitable process of numerical integration. Afterwards, they are transformed into the experimental coordinates using the relations shown in Eqs. (3) and (4). This allows a direct comparison to be made between the numerical and experimental results. The numerical calculation uses dimensionless variables that are introduced in the preceding journal article [1]. Where necessary, the dimensionless variables have been dimensionalised to allow a direct comparison between the numerical and experimental results. The figures shown in this section are only attributed to the numerical calculation, they need to be compared to the figures in the preceding Section 3.1. In Fig. 13 the numerically determined frequency responses for the coordinates θ_{n14} and θ_{n23} for the omnidirectional pendulum energy harvester in the low power take-off mode are shown. They are to be directly compared to experimental determined frequency responses Figs. 11(a) and 11(b). In Figs. 13(a) and 13(b) for the numerical calculation the omnidirectional pendulum

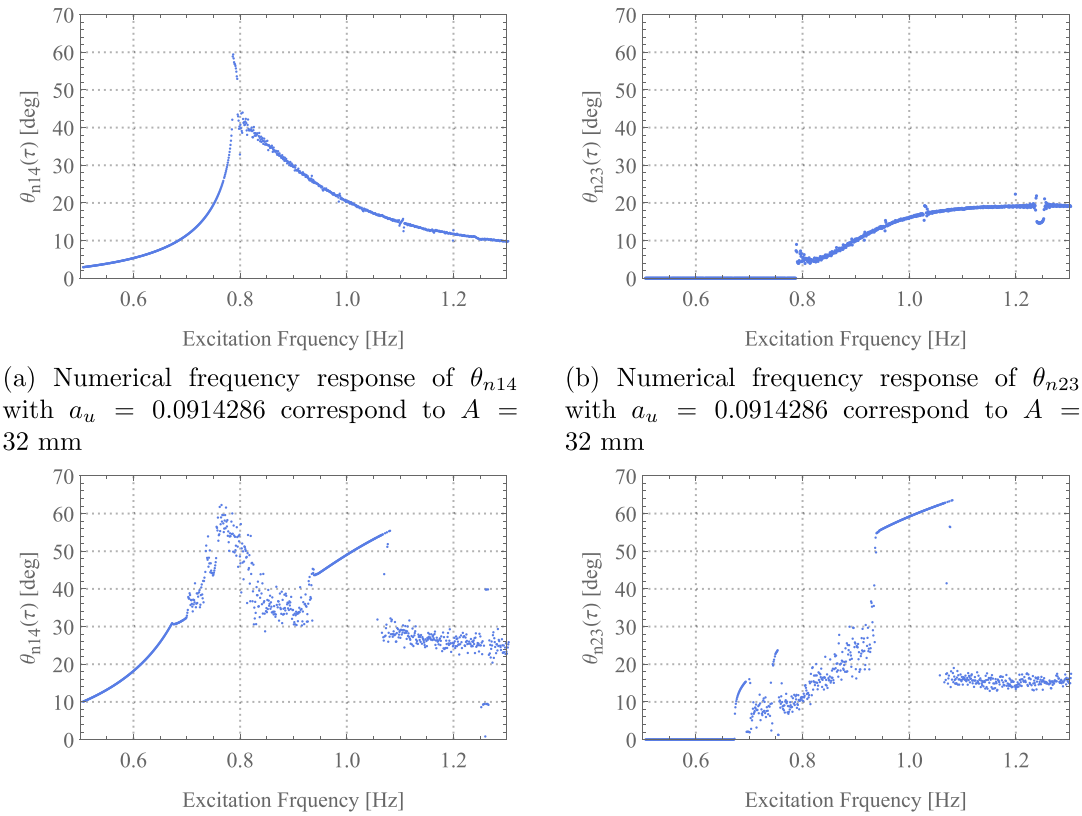

(a) Numerical frequency response of θ_{n14} with $a_u = 0.0914286$ correspond to $A = 32$ mm

(b) Numerical frequency response of θ_{n23} with $a_u = 0.0914286$ correspond to $A = 32$ mm

(c) Numerical frequency response of θ_{n14} with $a_u = 0.314286$ correspond to $A = 110$ mm

(d) Numerical frequency response of θ_{n23} with $a_u = 0.314286$ correspond to $A = 110$ mm

Fig. 13. Numerical frequency responses for the omnidirectional pendulum energy harvester. The dimensionless values for the numerical calculation are: $l = 0.35$ m, $m = 1.32$ kg, $g = 9.81\ \frac{\text{m}}{\text{s}^2}$, $\alpha_\theta = \alpha_\phi = 0.0712$, $a_v = a_w = 0$, $\epsilon_r = 0.01$, and $P_\theta = 0$.

energy harvester is excited with the same excitation amplitude as in the experiments. The experimental excitation amplitude of $A = 32$ mm is dimensionalised with the relations given in Eq. (7) and has therefore a value of $a_u = 0.0914286$. In the experimental section it was defined that the low power take-off mode is equivalent to a power output close to zero. Therefore, in the theoretical numerical observation of the lower power take-off mode the power take-off torque P_θ is set to zero as well.

The theoretical frequency response for the coordinate θ_{n14} is shown in Fig. 13(a). The energy harvester is excited with an excitation amplitude of $a_u = 0.0914286$ which is representative of a dimsensionalised excitation amplitude of $A = 32$ mm, see Eq. (7). For an excitation frequency from 0.5 Hz to 0.787 Hz the deflection of the coordinate θ_{n14} increases with approximately exponential characteristics. The maximum deflection of the coordinate θ_{n14} with a value of 59.42° is reached at an excitation frequency of 0.787 Hz. This is in accordance with the maximum of the linear frequency response in Fig. 11(a). With a further increase in the excitation the deflection of the coordinate θ_{n14} gradually decreases. Since the maximum deflection of the coordinate θ_{n14} is observed at a lower frequency value than the natural frequency an overall slight softening characteristics is visible.

In Fig. 13(b) the theoretical frequency response of the coordinate θ_{n23} where the energy harvester is excited with an excitation amplitude of $A = 32$ mm is shown. Until the excitation frequency of 0.789 Hz is exceeded the coordinate θ_{n23} does not show any deflection. In the range of excitation frequency from 0.789 Hz to 0.82 Hz the coordinate θ_{n23} shows similar characteristics to those of the experimentally determined frequency response in Fig. 11(b). With a further increase in the excitation frequency the deflection of the coordinate θ_{n23} continues to increase, and reaches a maximum deflection of 19.14°, without applying the outliers, for an excitation frequency of 1.24 Hz.

In Figs. 13(c) and 13(d) the excitation displacement amplitude is increased to a value of 110 mm. This high excitation amplitude is used only in the theoretical numerical model because of the physical and safety restrictions of the experimental rig it is unfortunately not feasible to conduct such high excitation amplitudes. The importance of the theoretical observation of such an excitation amplitude and the effect it has on the dynamics of the omnidirectional pendulum energy harvest is discussed in the following. It is noticeable that the dynamics of the system change with this increase in the excitation amplitude, see Fig. 13(c). For a range of excitation frequency from 0.5 Hz to 0.765 Hz the deflection of the coordinate increases. However, the theoretical frequency response does not show points that form a neat line after the excitation frequency of 0.70 Hz is exceeded and instead a range of different deflection values is visible. The maximum deflection of the coordinate θ_{n14} of 62.27° is reached at an excitation frequency of 0.765 Hz. With a further increase in the excitation frequency the deflection of the coordinate θ_{n14} decreases and reaches its local minimum for an excitation frequency of around 0.9 Hz. The deflection of the coordinate θ_{n14} continues to increase, with a further increase in the excitation frequency, and reaches a second local maximum of 55.43° at an excitation frequency of 1.08 Hz. With a further increase in the excitation frequency the deflection of the coordinate θ_{n14} jumps down to a value close to 30° and continues to slightly decrease in deflection with an increase in excitation frequency. This selection of the high excitation amplitude in the theoretical frequency response replicates the characteristics of the experimental frequency responses. It is especially interesting that a hardening effect (upper nonlinear jump region) is reproduced for the first time. For the selected experimental parameters in the numerical calculation the chosen excitation amplitude is the lowest one where these characteristics are visible. For any

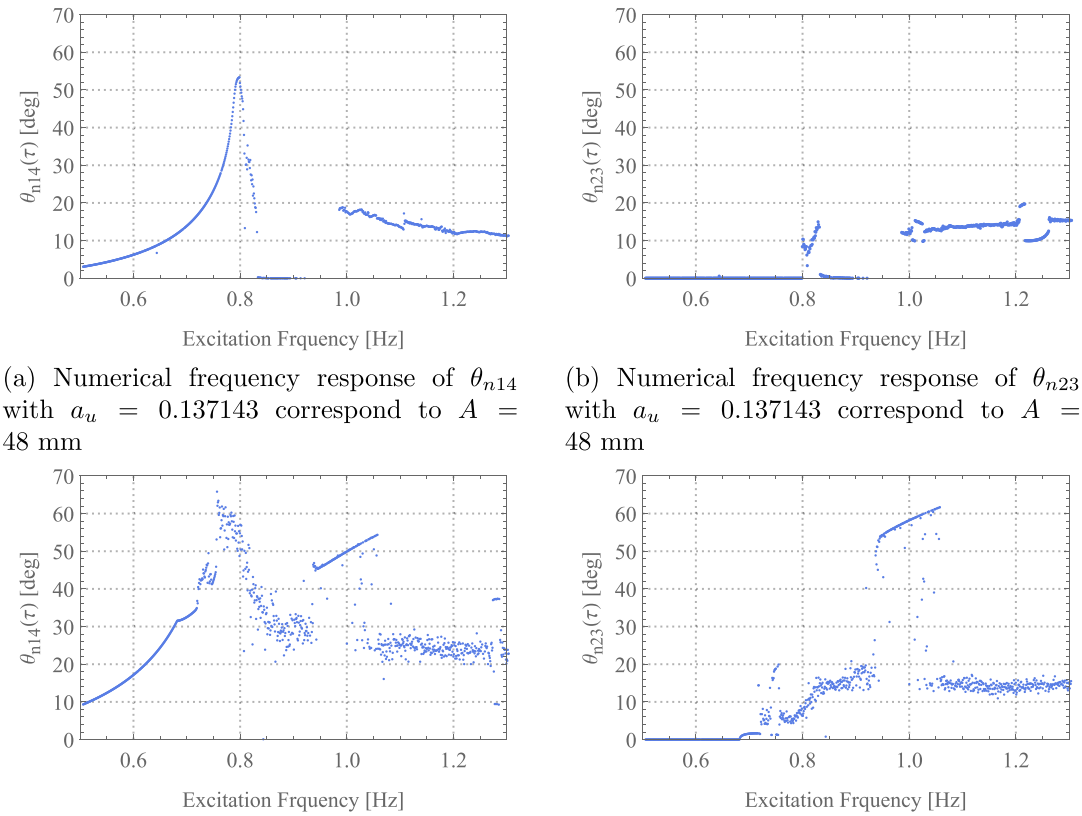

(a) Numerical frequency response of θ_{n14} with $a_u = 0.137143$ correspond to $A = 48$ mm

(b) Numerical frequency response of θ_{n23} with $a_u = 0.137143$ correspond to $A = 48$ mm

(c) Numerical frequency response of θ_{n14} with $a_u = 0.314286$ correspond to $A = 110$ mm

(d) Numerical frequency response of θ_{n23} with $a_u = 0.314286$ correspond to $A = 110$ mm

Fig. 14. Numerical frequency responses for the omnidirectional pendulum energy harvester. The dimensionless values for the numerical calculation are: $l = 0.35$ m, $m = 1.32$ kg, $g = 9.81\ \frac{\text{m}}{\text{s}^2}$, $\alpha_\theta = \alpha_\phi = 0.0712$, $a_v = a_w = 0$, $\epsilon_r = 0.01$, and $P_\theta = 0.0375092$.

lower selected excitation amplitudes the hardening effect is not visible in the numerical calculation.

In Fig. 13(d) the theoretical frequency response for the coordinate θ_{n23} with an excitation amplitude of $A = 110$ mm is shown. Until the excitation frequency of 0.673 Hz is exceeded the coordinate θ_{n23} does not show any deflection. In the range of the excitation frequencies from 0.673 Hz to 0.76 Hz the coordinate θ_{n23} shows deflections that appear not to follow any clear structure, similar to those in the experimentally determined results. With a further increase in the excitation frequency the deflection of the coordinate θ_{n23} increases and jumps up to a deflection value of 54.43° at an excitation frequency of 0.937 Hz. The deflection of the coordinate θ_{n23} continues to increase and reaches its maximum deflection of 63.54° at a value of the excitation frequency of 1.08 Hz. This is at the same position as the second local maximum of the coordinate θ_{n14}. The numerical calculation therefore shows the upper nonlinear jump region similar to the experimental results. With a further increase in the excitation frequency the deflection of the coordinate θ_{n23} jumps down to a value of around 15° and continues to slightly decrease as the excitation frequency increases onwards from there.

In Fig. 14 the numerical frequency responses for the pendulum energy harvester in the high power take-off mode are shown. For this, the damping ratio of the low power take-off mode is used and the level of the power take-off torque is increased to simulate a higher power take-off. The power take-off torque is selected by adapting the maximum deflection of the experimental frequency response in Fig. 12(a) with the numerical frequency response in Fig. 14(a) to a similar deflection level. This is done with multiple iterations to find the closest fit. The selected power take-off torque has a value of $P_\theta = 0.0375092$ which is equivalent to 0.17 N m. This power take-off torque is subsequently selected for all the following theoretical frequency responses in Fig. 14. The examination of different excitation amplitudes similar to the one in Fig. 13 is used here as well. The theoretical frequency response of the coordinate θ_{n14} with an excitation amplitude of $A = 48$ mm is shown in Fig. 14(a) . This is the same excitation amplitude as in the experimental evaluation of the omnidirectional pendulum energy harvester in the high power take-off mode. The deflection of the coordinate θ_{n14} increases with an approximately exponential characteristic until reaching a maximum deflection of 53.35° for a value of the excitation frequency of 0.799 Hz. This is at the same position as the maximum deflection of the linear part of the frequency response in the high power take-off mode, see Fig. 12(a). With a further increase in the excitation frequency the deflection of the coordinate θ_{n14} decreases drastically and the deflection completely disappears for a range of the excitation frequency from 0.83 Hz to 0.98 Hz. The deflection of the coordinate θ_{n14} jumps down to a value of 17.94° and decreases from there on, with an increase in the excitation frequency.

Fig. 14(b) shows the theoretical frequency response for the coordinate θ_{n23}. The frequency response does not show a deflection of the coordinate θ_{n23} for ranges of the excitation frequencies from 0.5 Hz to 0.7 Hz and from 0.83 Hz to 0.984 Hz. In the range of excitation frequency from 0.8 Hz to 0.83 Hz the coordinate shows deflection values similar to the experimental values observed in this region. For an excitation frequency from 0.984 Hz to 1.3 Hz the deflection of the coordinate θ_{n23} shows a deflection where the trend slightly increases with an increase in the excitation frequency. In some excitation frequency regions outliers can also be observed.

In Fig. 14(c) the theoretical frequency response of the coordinate θ_{n14} with a high excitation amplitude of $A = 110$ mm is shown. As before

this only theoretical increase is done to show the upper nonlinear jump region of the experimental frequency responses. The deflection of the coordinate θ_{n14} increases for a range of excitation frequency from 0.5 Hz to 0.757 Hz where it reaches the maximum deflection of 65.81°. With a further increase in the excitation frequency the deflection of the coordinate θ_{n14} decreases and shows a local maximum at a value of the excitation frequency of around 0.88 Hz. The deflection continues to increase with a further increase in the excitation frequency and jumps up to a higher deflection value of 46.02° for an excitation frequency of 0.93 Hz. With a further increase in the excitation frequency the deflection of the coordinate θ_{n14} continues to increase and shows a second local maximum of 54.46° for the excitation frequency of 1.06 Hz. The deflection of the coordinate θ_{n14} jumps down to a deflection value of around 25° with a further increase in the excitation frequency and continues to decrease in value onwards from there.

The theoretical frequency response of the coordinate θ_{n23} with an increased excitation amplitude of $A = 110$ mm is shown in Fig. 14(d). Until the excitation frequency of 0.679 Hz is exceeded the coordinate θ_{n23} does not show any deflection. In the range of excitation frequencies from 0.72 Hz to 0.77 Hz the coordinate θ_{n23} shows deflection values that show a local maximum. The experimental results show similar characteristics. With a further increase in the excitation frequency the deflection of the coordinate θ_{n23} continues to increase and jumps up to a higher deflection value of 54.07° for the value of the excitation frequency of 0.948 Hz. The deflection continues to increase onwards and shows its maximum deflection of 61.68° at an excitation frequency of 1.06 Hz. With a further increase in the excitation frequency the deflection of the coordinate θ_{n23} jumps down to a value of around 15° and continues to show similar deflection values for the rest of the excitation frequency range.

It is evident that with an increase in the excitation amplitude the characteristics of the experimental results can be reproduced well. For the theoretical frequency response of the coordinate θ_{n14} the two local maxima with the minimum in between are clearly visible. Additionally, the upper nonlinear jumping regions are clearly visible for both of the coordinates θ_{n14} and θ_{n23}.

4. Conclusions

The introduced omnidirectional pendulum energy harvester was examined experimentally for different power take-off modes and the results were compared with numerical calculations. A broadening effect of the operational range of the energy harvester has been observed and the base value to which the results are referred to was defined at the beginning of the results section. This broadening effect is mostly attributed to the upper nonlinear sweep region which increases the deflections of both shafts drastically. The upper nonlinear sweep region broadens the operational range of the coordinate θ_{14} for the low power take-off by 109.06% and for the high power take-off mode by 55.0%. For the coordinate θ_{23} the up-sweep broadens the operational range of the energy harvester in the low power take-off mode by 109.06% and in the high power take-off mode by 61.36%. The down-sweep broadens the operational range of the coordinate θ_{14} in the low power take-off mode by 21.25% and in the high power take-off mode by 4.54%. Therefore the operational area of the coordinate θ_{14} can overall be increased by 130.31% in the low power take-off mode and by 59.55% in the high power take-off mode. The optimum operational point is located at the maximum deflection of the upper nonlinear jump region where both shafts show high deflection values. The optimum operational point has the highest voltage output at this point because of the higher velocity of the pendulum bob that is present. To reach this point an initial excitation frequency between the two local maxima in the linear frequency response of the coordinate θ_{14} has to be selected from where an up-sweep of the excitation frequency is performed. The numerical comparison of the experimental results with the exact excitation amplitude unfortunately does not show the same characteristics as the experiment. However, an increase in the excitation amplitude shows all the characteristics of the experimental results well. These characteristics include the two local maxima and the local minimum in between for the coordinate θ_{n14}. Additionally, both numerically determined coordinates θ_{n14} and θ_{n23} show a representation of the upper nonlinear jump region similar to the upper nonlinear jump region observed for the experimental examination of the omnidirectional pendulum energy harvester.

5. Further research

When transferring the in this work examined experiment into a real live application the excitational forces are subject to change. The excitations the energy harvester would be exposed to would be predominantly random, therefore the approach of Stochastic Resonance is most likely to be used, for further information on this see [36,37].

Additionally, energy harvesting based on the principle of double hopf jumping dynamic is subject to stability loss particularly under random excitation. Therefore, it is crucial that such a system is subject to a careful analysis of stochastic stability. Work on this has been done by [38,39].

Declaration of competing interest

The authors declare that they have no known competing financial interests or personal relationships that could have appeared to influence the work reported in this paper.

Data availability

Data will be made available on request.

References

[1] P. Sommermann, M.P. Cartmell, The dynamics of an omnidirectional pendulum harvester, Nonlinear Dynam. (2021) 1–12, http://dx.doi.org/10.1007/s11071-021-06479-z.
[2] D. Watt, M.P. Cartmell, An externally loaded parametric oscillator, J. Sound Vib. 170 (3) (1994) 339–364, http://dx.doi.org/10.1006/jsvi.1994.1067.
[3] M. McRobb, Development and Enhancement of Various Mechanical Oscillators for Application in Vibrational Energy Harvesting (Ph.D. thesis), University of Glasgow, 2014.
[4] J.W. Miles, Stability of forced oscillations of a spherical pendulum, Quart. Appl. Math. 20 (1) (1962) 21–32, http://dx.doi.org/10.1090/qam/133521.
[5] J. Miles, Resonant motion of a spherical pendulum, Physica D 11 (3) (1984) 309–323, http://dx.doi.org/10.1016/0167-2789(84)90013-7.
[6] J. Miles, Internal resonance of a detuned spherical pendulum, ZAMP Z. Angew. Math. Phys. 36 (4) (1985) 609–615, http://dx.doi.org/10.1007/BF00945300.
[7] J.W. Miles, Q.P. Zou, Parametric excitation of a detuned spherical pendulum, J. Sound Vib. 164 (2) (1993) 237–250, http://dx.doi.org/10.1006/jsvi.1993.1211.
[8] M.G. Olsson, The precessing spherical pendulum, Amer. J. Phys. 46 (11) (1978) 1118–1119, http://dx.doi.org/10.1119/1.11151.
[9] M.G. Olsson, Spherical pendulum revisited, Amer. J. Phys. 49 (6) (1981) 531–534, http://dx.doi.org/10.1119/1.12666.
[10] D.J. Tritton, Ordered and chaotic motion of a forced spherical pendulum, Eur. J. Phys. 7 (3) (1986) 162–169, http://dx.doi.org/10.1088/0143-0807/7/3/003.
[11] A.P. Markeyev, The dynamics of a spherical pendulum with a vibrating suspension, J. Appl. Math. Mech. 63 (2) (1999) 205–211, http://dx.doi.org/10.1016/S0021-8928(99)00028-3, URL www.elsevier.com/locate/jappmat.
[12] S. Pospíšil, C. Fischer, J. Náprstek, Experimental analysis of the influence of damping on the resonance behavior of a spherical pendulum, Nonlinear Dynam. 78 (1) (2014) 371–390, http://dx.doi.org/10.1007/s11071-014-1446-6.
[13] P.J. Bryant, Breakdown to chaotic motion of a forced, damped, spherical pendulum, Physica D 64 (1–3) (1993) 324–339, http://dx.doi.org/10.1016/0167-2789(93)90263-Z.
[14] D.D. Kana, D.J. Fox, Distinguishing the transition to chaos in a spherical pendulum, Chaos 5 (1) (1995) 298–310, http://dx.doi.org/10.1063/1.166077.
[15] J.H. Cartwright, D.J. Tritton, Chaotic dynamics and reversal statistics of the forced spherical pendulum: Comparing the Miles equations with experiment, Dyn. Syst. 25 (1) (2010) 1–16, http://dx.doi.org/10.1080/14689360902751574.
[16] J. Náprstek, C. Fischer, Types and stability of quasi-periodic response of a spherical pendulum, Comput. Struct. 124 (2013) 74–87, http://dx.doi.org/10.1016/j.compstruc.2012.11.003.

[17] G. Litak, J. Margielewicz, D. Gąska, D. Yurchenko, K. Dąbek, Dynamic response of the spherical pendulum subjected to horizontal Lissajous excitation, Nonlinear Dynam. (2020) 1–18, http://dx.doi.org/10.1007/s11071-020-06023-5.

[18] A.Y. Leung, J.L. Kuang, On the chaotic dynamics of a spherical pendulum with a harmonically vibrating suspension, Nonlinear Dynam. 43 (3) (2006) 213–238, http://dx.doi.org/10.1007/s11071-006-7426-8.

[19] N. Elvin, A. Erturk, Introduction and Methods of Mechanical Energy Harvesting, Vol. 9781461457, Springer New York, 2013, pp. 3–14, http://dx.doi.org/10.1007/978-1-4614-5705-3_1.

[20] R.J. Vullers, R. van Schaijk, I. Doms, C. Van Hoof, R. Mertens, Micropower energy harvesting, Solid-State Electron. 53 (7) (2009) 684–693, http://dx.doi.org/10.1016/j.sse.2008.12.011.

[21] H. Shen, J. Qiu, M. Balsi, Vibration damping as a result of piezoelectric energy harvesting, Sensors Actuators A 169 (2011) 178–186, http://dx.doi.org/10.1016/j.sna.2011.04.043.

[22] X.-R. Chen, T.-Q. Yang, W. Wang, X. Yao, Vibration energy harvesting with a clamped piezoelectric circular diaphragm, 2011, http://dx.doi.org/10.1016/j.ceramint.2011.04.099, URL www.elsevier.com/locate/ceramint.

[23] J. Elmes, V. Gaydarzhiev, A. Mensah, K. Rustom, J. Shen, I. Batarseh, Maximum energy harvesting control for oscillating energy harvesting systems, in: PESC Record - IEEE Annual Power Electronics Specialists Conference, 2007, pp. 2792–2798, http://dx.doi.org/10.1109/PESC.2007.4342461.

[24] M. Borowiec, G. Litak, A. Rysak, P.D. Mitcheson, T.T. Toh, Dynamic response of a pendulum-driven energy harvester in the presence of noise, J. Phys. Conf. Ser. 476 (1) (2013) 0–5, http://dx.doi.org/10.1088/1742-6596/476/1/012038.

[25] M. Cartmell, J. Lawson, Performance enhancement of an autoparametric vibration absorber by means of computer control, J. Sound Vib. 177 (2) (1994) 173–195, http://dx.doi.org/10.1006/jsvi.1994.1426.

[26] Energy harvesting from pendulum oscillations, Int. J. Non-Linear Mech. 94 (March) (2017) 251–256, http://dx.doi.org/10.1016/j.ijnonlinmec.2017.03.022.

[27] C. Liang, Y. Wu, L. Zuo, Broadband pendulum energy harvester, Smart Mater. Struct. 25 (9) (2016) 095042, http://dx.doi.org/10.1088/0964-1726/25/9/095042, URL https://iopscience.iop.org/article/10.1088/0964-1726/25/9/095042.

[28] J. Graves, Y. Kuang, M. Zhu, Scalable pendulum energy harvester for unmanned surface vehicles, Sensors Actuators A 315 (2020) 112356, http://dx.doi.org/10.1016/j.sna.2020.112356.

[29] A. Zhang, V. Sorokin, H. Li, Energy harvesting using a novel autoparametric pendulum absorber-harvester, J. Sound Vib. 499 (2021) 116014, http://dx.doi.org/10.1016/j.jsv.2021.116014.

[30] T. Anurakpandit, N.C. Townsend, P.A. Wilson, The numerical and experimental investigations of a gimballed pendulum energy harvester, Int. J. Non-Linear Mech. 120 (2020) 103384, http://dx.doi.org/10.1016/j.ijnonlinmec.2019.103384.

[31] T. Wang, H. Lou, S. Zhu, Prototyping and electromagnetic analysis of a biaxial-pendulum wave energy harvester, in: OCEANS 2021: San Diego – Porto, IEEE, 2022, pp. 1–5, http://dx.doi.org/10.23919/oceans44145.2021.9706060, URL https://ieeexplore.ieee.org/document/9706060/.

[32] P. Sommermann, An Experimental and Theoretical Study of an Omnidirectional Pendulum Energy Harvester (Ph.D. thesis), University of Strathclyde, 2023, http://dx.doi.org/10.48730/VHDW-XR54, URL https://stax.strath.ac.uk/concern/theses/3n203z60c?locale=en.

[33] P.C. Tan, R.E. Morrison, D.G. Holmes, Voltage form factor control and reactive power compensation in a 25-kV electrified railway system using a shunt active filter based on voltage detection, IEEE Trans. Ind. Appl. 39 (2) (2003) 575–581, http://dx.doi.org/10.1109/TIA.2003.809455.

[34] I. Boldea, Electric Generators Handbook - Two Volume Set, CRC Press, 2018, http://dx.doi.org/10.1201/9781315214191.

[35] J. Pyrhönen, T. Jokinen, V. Hrabovcová, Design of Rotating Electrical Machines, John Wiley & Sons Ltd, Chichester, UK, 2013, http://dx.doi.org/10.1002/9781118701591, URL http://doi.wiley.com/10.1002/9781118701591.

[36] Stochastic Resonance: From Suprathreshold Stochastic Resonance to Stochastic Signal Quantization, Vol. 9780521882620, Cambridge University Press, 2008, pp. 1–425, http://dx.doi.org/10.1017/CBO9780511535239.

[37] J. Náprstek, Stochastic resonance: Challenges to engineering dynamics, Comput. Technol. Rev. 12 (2015) 53–101, http://dx.doi.org/10.4203/CTR.12.3.

[38] J. Náprstek, C. Fischer, Auto-parametric semi-trivial and post-critical response of a spherical pendulum damper, Comput. Struct. 87 (2009) 1204–1215, http://dx.doi.org/10.1016/J.COMPSTRUC.2008.11.015.

[39] J. Náprstek, S. Pospíšil, J.D. Yau, Stability of two-degrees-of-freedom aero-elastic models with frequency and time variable parametric self-induced forces, J. Fluids Struct. 57 (2015) 91–107, http://dx.doi.org/10.1016/J.JFLUIDSTRUCTS.2015.05.010.